

# Using Continuous GWs from Known Pulsars to Measure Gravitational Wave Speed

## Final Project Report

Jake Mattinson (Caltech)  
Mentors: Alan Weinstein (Caltech), Max Isi (Caltech)  
LIGO SURF 2016

October 29, 2016

### Abstract

Gravitational waves provide a unique opportunity to test the strong-field highly-dynamical regime of Einstein's General Theory of Relativity. In this project, we explored the possibility of detecting deviations from Einstein's predictions by examining the speed of gravitational waves. We have studied continuous gravitational waves in order to determine whether it will be possible to place a limit on deviations from the general-relativistic prediction of the speed of the waves. We estimate the magnitude of constraints on deviations from the speed of light by means of a Bayesian analysis of simulated data corresponding to different sources.

## 1 Project Description

Gravitational waves (GWs) were predicted by Einstein in 1916 as a part of his development of the Theory of General Relativity (GR) and finally detected directly in September 2015 by the Laser Interferometer Gravitational wave Observatory (LIGO) [1]. Now that we have observed this phenomenon directly, we can start to analyze its properties in more depth. We attempt to measure the speed of GWs by looking at continuous waves (CWs).

Our method is based on the observation of the small frequency modulation of these long-lived signals. This is done by analyzing months of data and searching for modulation of long-term GW signals due to Doppler shifts with periodicity of a sidereal day for different sources. We therefore avoid transient sources like the black hole mergers that have already been observed, and focus on possible sources of gravitational waves which would have longer and more stable emissions. These sources, primarily rotating neutron stars (e.g. pulsars), are expected to emit CW signals with very stable frequencies and long durations but small amplitudes. This research will focus on known pulsars which could emit CWs, with timing data from the TEMPO2 software [2]. Known

pulsars are listed in the Australia Telescope National Facility pulsar catalogue (ATNF) [3]. The ATNF catalogue lists 2536 known pulsars, 291 of which are within the LIGO bandwidth (rotating at over 15 Hz, yielding GWs at 30 Hz).

An observer stationary relative to the source would observe the wave as a simple sinusoid, but due to the detector’s motion relative to the source there is a significant frequency modulation due to Doppler-like effects. There exist multiple, well-established methods to look for CW signals in LIGO data [4, 5, 6]. However, most of those signal searches assume the GR result that gravitational waves travel at the speed of light. A variation from that speed has not been well explored in the context of these searches.

## 2 Problem Description

In order to use the Doppler shifts of the signal to measure the speed of gravitational waves, we must understand all of the different effects which shape a wave before it gets to us. In this analysis, we primarily consider the source’s spin, the detector motion with respect to the source, and the detector orientation.

First, we need to understand how the signal measured at the detector relates to the motion of the source. It can be shown that GR predicts that a triaxial neutron star emits GWs at twice the spin frequency [7], i.e.

$$\nu_{\text{GW}} = 2\nu_{\text{spin}}. \quad (1)$$

The source is expected to emit a sinusoidal signal with some amplitude,  $A$ , dependent upon the physical characteristics of the source and the distance between the observer and the source:

$$h(t_p) = A \sin(\theta(t_p)). \quad (2)$$

Here,  $t_p$  (the “pulsar time”) is the time as measured with a clock at rest with respect to the source.  $\theta(t_p)$  can be Taylor-expanded using eq. (1) to yield:

$$\theta(t_p) = \theta_0 + 4\pi \left( \nu t_p + \frac{1}{2} \dot{\nu} t_p^2 + \frac{1}{6} \ddot{\nu} t_p^3 \right), \quad (3)$$

where  $\theta_0$  is a fiducial phase measured at an arbitrary starting time and a dot indicates time derivatives. Because we can infer the rate of the actual rotation of the source from its radio emission (from [3, 2]), we know these parameters incredibly well. Younger pulsars will often have unexplained jumps in their frequency that will quickly die down, called glitches; these must be taken into account for a more accurate picture of the waveform than the above analytical model.

Next, we need to understand the sensitivity of the detector. Unlike a telescope, which is movable and has a limited observation region, LIGO is sensitive to signals from every direction and cannot be aimed. This means that the detectors should be modeled like antennas which have sensitivity depending on the polarization of the signal, the location of the source, and the orientation of

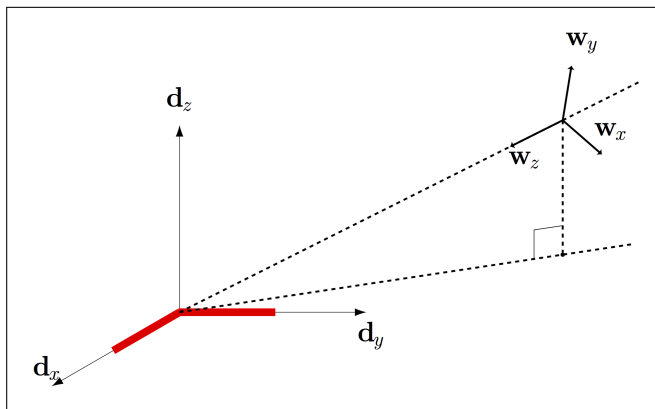


Figure 1: This image shows the definitions of the vectors which define the source-detector system. Note that  $\mathbf{w}_z = \mathbf{w}_x \times \mathbf{w}_y$ . Detector arms (thick red) lie parallel to  $\mathbf{d}_x$  and  $\mathbf{d}_y$ , while  $\mathbf{d}_z$  points to the local zenith.

the detector. We can define a set of vectors which characterize the detector:  $\mathbf{d}_z$  points from the center of the Earth to the detector,  $\mathbf{d}_x$  and  $\mathbf{d}_y$  are unit vectors that point along its arms. We then define the orientation of the pulsar with unit vectors:  $\mathbf{w}_z$  is the unit vector from the source toward the detector,  $\mathbf{w}_x$  points along the local East orientation, and  $\mathbf{w}_y$  is perpendicular to both of those at a local North. The local directions have a rotation relative Earth's coordinates of angle  $\psi$  which is taken from ATNF [3]. This can be seen in Fig. 1.

GR predicts that CWs have two polarizations: plus (+) and cross ( $\times$ ). Waves with these polarizations stretch spacetime perpendicular to their direction of propagation: shrinking it in one direction and expanding it in the other. These two polarizations are almost the same, excepting a  $45^\circ$  rotation from one to the other (hence their names). The detector sensitivity to each will be different, based on the geometry of the setup. Using the above definitions, we can derive the following sensitivities, or antenna patterns (APs), for each polarization:

$$F_+ = \frac{1}{2} [(\mathbf{w}_x \cdot \mathbf{d}_x)^2 - (\mathbf{w}_x \cdot \mathbf{d}_y)^2 - (\mathbf{w}_y \cdot \mathbf{d}_x)^2 + (\mathbf{w}_y \cdot \mathbf{d}_y)^2], \quad (4)$$

$$F_\times = (\mathbf{w}_x \cdot \mathbf{d}_x)(\mathbf{w}_y \cdot \mathbf{d}_x) - (\mathbf{w}_x \cdot \mathbf{d}_y)(\mathbf{w}_y \cdot \mathbf{d}_y). \quad (5)$$

Because the position of the observatory changes due to the rotation of Earth, the antenna pattern for a particular sky location varies across a sidereal day and affects the amplitude of the signal, leading to a characteristic amplitude modulation (AM). In fact, eqs. (4,5), if expanded analytically in the detector frame, can be written as trigonometric functions in terms of twice the azimuthal angles of the source with respect to the interferometer, i.e. we will expect a period of half a day as well as a full day (diurnal) cycle.

From this, we want to understand what the AM does to a signal. Generally, the strain can be written as the sum

$$h(t) = h_+(t) \cos \theta(t) + h_\times(t) \sin \theta(t), \quad (6)$$

where  $h_+$  and  $h_\times$  are the magnitudes of strain in each polarization. Combining this with the system geometry and the APs yields the equation:

$$h(t) = h_0 \left( \frac{1 + \cos^2 \iota}{2} F_+(t) \cos(t) + \cos \iota F_\times(t) \sin(t) \right), \quad (7)$$

$\iota$  is the angle of inclination of the source relative the detector and  $h_0$  is the total strain.

This equation can be decomposed into a set of complex exponentials (using analytical definitions of sine and cosine) yielding:

$$h(t) = \Lambda(t)e^{i\theta(t)} + \Lambda^*(t)e^{-i\theta(t)}, \quad (8)$$

where

$$\Lambda(t) = h_0 \left( \frac{1 + \cos^2 \iota}{4} F_+(t) + \frac{i \cos \iota}{2} F_\times(t) \right). \quad (9)$$

$\Lambda(t)$  now represents the AM signal due to the APs.

However, we still need to consider both the Doppler and relativistic delays, as the interferometers are moving relative to the source. This impacts the above equation, as eq. (3) refers to the time measured at a point stationary relative the source. Therefore, in eqs. (6 - 9),  $\theta(t)$  could be written as  $\theta(t_p(t))$  with  $t$  being time measured by a clock placed at the detector.

From here on, we assume that the distance between the pulsar and the Solar System Barycenter (SSB) is constant; i.e.  $t_p - t_b$  is constant. Therefore, we will be measuring time relative the SSB with  $t_b$ , as a proxy for time at the pulsar itself,  $t_p$ . For a general pulsar, we can express the barycentric time as the sum:

$$t_b \equiv t_b(t) = t + \Delta_E + \Delta_S + \Delta_{Bi} + \Delta_R, \quad (10)$$

where  $t_b$  is the time measured from the Solar System Barycenter (SSB),  $t$  is the time measured on Earth,  $\Delta_E$  is the Einstein delay due to Special Relativity,  $\Delta_S$  is the solar system Shapiro delay from GR,  $\Delta_{Bi}$  is the binary Shapiro delay and  $\Delta_R$  is the Rømer delay due to the time it takes the wave to reach the observatory.  $\Delta_E$  is practically constant in relevant timescales, so it is ignorable.  $\Delta_S$  is of order  $10^{-7}s$  [8], far below our time resolution, making it ignorable. We will focus on pulsars outside of binaries, so we will not have a  $\Delta_{Bi}$  term. We only have to calculate the Rømer delay. This is given by the formula:

$$\Delta_R = \frac{\mathbf{r} \cdot \hat{\mathbf{n}}}{c_g}, \quad (11)$$

where  $\mathbf{r}$  points from the SSB to the detector,  $\hat{\mathbf{n}}$  is the unit vector pointing from the SSB to the source, and  $c_g$  is the speed of the gravitational wave. We will

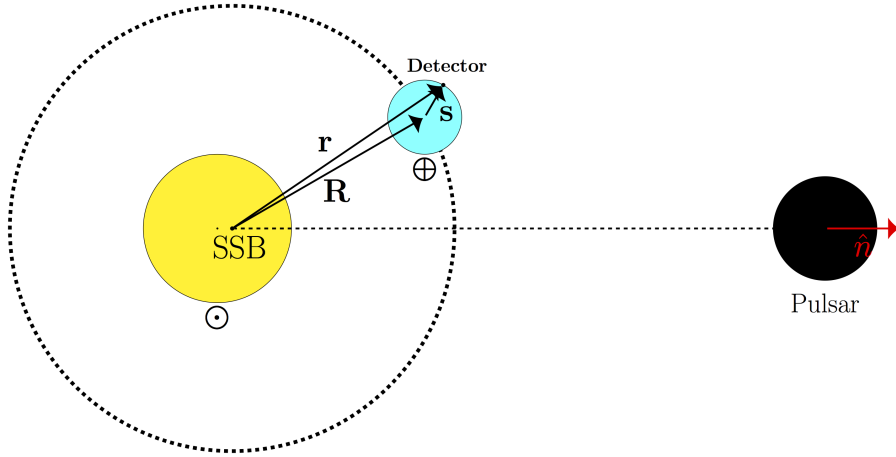


Figure 2: Geometry of the Rømer delay.

assume  $\hat{\mathbf{n}}$  is constant, as the source is effectively at rest relative the SSB. We know  $\mathbf{r}$  has two components:  $\mathbf{r} = \mathbf{R} + \mathbf{s}$ , where  $\mathbf{R}$  points from the SSB to the center of Earth and  $\mathbf{s}$  points from Earth to the detector, as seen in Figure 2.  $\mathbf{R}$  oscillates over a year while  $\mathbf{s}$  has periodicity of a sidereal day.

For a sense of scale, the speed that a point on Earth's equator moves as it rotates ( $|d\mathbf{s}/dt|$ ) is about  $465.1 \text{ m/s} = 1.55 \times 10^{-6} c$  while the speed that Earth orbits the Sun ( $|d\mathbf{R}/dt|$ ) is about  $29,800 \text{ m/s} = 9.9 \times 10^{-5} c$ , about 2 orders of magnitude larger.

The Rømer delay is where the speed of the gravitational wave comes into play as its time dependence induces an observable frequency modulation (FM). This, again, distorts our signal in a way that, unlike the AM, depends on the speed of the wave. Currently, the LIGO Algorithm Library (`LALSuite`) assumes that  $c_g = c$ , as this is what GR predicts [9].

We now know how to model a wave with all of the applicable dynamics (AM and FM). Now that the wave has traveled to the detector, the raw data goes through a long process in order to search for a signal. For continuous waves with a known source, the procedure is the following:

- 1. Raw data is collected**

This step is beyond the scope of this project, but it suffices to mention that the data is dominated by noise and is sampled at  $f_s = 16,384 \text{ Hz}$ .

- 2. Heterodyne**

To measure the gravitational wave speed, we want to isolate the AM of the signal, so we want to heterodyne the data using the phase evolution obtained from radio observations. This process generally removes a high

frequency signal leaving a much lower one; in this case, we will use it to take out the oscillation of the wave seen in eqs. (2) & (3).

In keeping with eq. (8), heterodyning can isolate  $\Lambda(t)$ . The process simply takes the calibrated strain and multiplies it by  $e^{-i\theta(t)}$  to get:

$$h_{\text{het}}(t) = e^{-i\theta(t)} \cdot h(t) = \Lambda(t) + \Lambda^*(t)e^{-2\theta(t)}, \quad (12)$$

which yields a very low frequency term and a very high frequency one. For the Crab Pulsar, these would have frequencies of about 0.00002 Hz (an inverse sidereal day) and 120 Hz (as the Crab rotates at about 30 Hz), respectively. It may be important to note here that even though the initial data was purely real valued, we are now working in the complex domain.

It should also be mentioned that since the Rømer delay is implemented in this step, this pre-processing may reveal the difference in speed, since current implementations assume the speed of gravitational waves,  $c_g$ , equals the speed of light,  $c$ . This is the key to this study. If that assumption is not true and  $c_g \neq c$ , then eq. (12) does not hold. We can define  $\theta(t; v)$  for some speed of gravitational wave  $v$  and let  $\delta\theta(t) = \theta(t; c_g) - \theta(t; c)$ . When we try to heterodyne assuming  $c_g = c$ , we are left with

$$h'_{\text{het}}(t) = \Lambda(t)e^{i\delta\theta(t)} + \Lambda^*(t)e^{-i(\theta(t; c_g) + \theta(t; c))}. \quad (13)$$

The second term gets removed during the filtering, but the first term keeps the  $\delta\theta$  term. That can be easily calculated using eqs. (3), (10), and (11):

$$\delta\theta(t_b) = \theta(t_b; c_g) - \theta(t; c) \quad (14)$$

$$= \theta_0 + 4\pi \left[ \nu t_{b, \text{GW}} + \frac{1}{2} \dot{\nu} t_{b, \text{GW}}^2 + \frac{1}{6} \ddot{\nu} t_{b, \text{GW}}^3 \right] - \theta_0 - 4\pi \left[ \nu t_{b, c} + \frac{1}{2} \dot{\nu} t_{b, c}^2 + \frac{1}{6} \ddot{\nu} t_{b, c}^3 \right] \quad (15)$$

$$= 4\pi \left[ \nu \cdot (t_{b, \text{GW}} - t_{b, c}) + \frac{1}{2} \dot{\nu} \cdot (t_{b, \text{GW}}^2 - t_{b, c}^2) + \frac{1}{6} \ddot{\nu} \cdot (t_{b, \text{GW}}^3 - t_{b, c}^3) \right] \quad (16)$$

$$= \left( \frac{1}{c_g} - \frac{1}{c} \right) (\mathbf{r} \cdot \hat{\mathbf{n}}) (\nu + \dot{\nu} t + \frac{1}{2} \ddot{\nu} t^2) + \left( \frac{1}{c_g^2} - \frac{1}{c^2} \right) (\mathbf{r} \cdot \hat{\mathbf{n}})^2 \left( \frac{\dot{\nu}}{2} + \frac{\ddot{\nu}}{2} t \right) + \left( \frac{1}{c_g^3} - \frac{1}{c^3} \right) (\mathbf{r} \cdot \hat{\mathbf{n}})^3 \frac{\ddot{\nu}}{6} \quad (17)$$

$$= \left( \frac{1}{c_g} - \frac{1}{c} \right) (\mathbf{r} \cdot \hat{\mathbf{n}}) \nu(t) + \left( \frac{1}{c_g^2} - \frac{1}{c^2} \right) (\mathbf{r} \cdot \hat{\mathbf{n}})^2 \frac{\dot{\nu}(t)}{2} + \left( \frac{1}{c_g^3} - \frac{1}{c^3} \right) (\mathbf{r} \cdot \hat{\mathbf{n}})^3 \frac{\ddot{\nu}(t)}{6} \quad (18)$$

Defining  $\beta, \kappa$  such that  $c_g = \beta c$  and  $\mathbf{r} \cdot \hat{\mathbf{n}} = \kappa$ , this simplifies to

$$\delta\theta(t) = c^{-1} (\beta^{-1} - 1) \kappa \nu(t) + \frac{c^{-2}}{2} (\beta^{-2} - 1) \kappa^2 \dot{\nu}(t) + \frac{c^{-3}}{6} (\beta^{-3} - 1) \kappa^3 \ddot{\nu}(t),$$

$$\delta\theta(t) = \sum_{i=1}^3 \frac{c^{-i}(\beta^{-i} - 1)}{i!} \cdot \kappa^i \cdot \frac{d^i\theta(t)}{dt^i}. \quad (19)$$

In this step, the phase evolution information from radio emission is used. The synchronization between GW and radio data implicitly assumes  $c_g = c$  because we think the arrival of gravitational waves and any EM counterparts should roughly coincide. If the  $c_g$  is very different from  $c$ , this may render signals invisible at times, but this project assumes a small deviation, as predicted in most theories [4]. The sensitivity to this deviation needs to be explored in further research.

### 3. Filters (e.g. Butterworth) applied

This low pass filter (LPF) removes high frequency features.

### 4. Downsample

Downsampling serves as another LPF, which suppresses higher frequency signals, so the second term in eq. (13) is removed. As the name implies, downsampling involves reducing the number of points in the data being analyzed. To do this for CWs, LIGO takes one minute sized chunks and takes their average. This means that from the heterodyned signal, indexed by  $i$ , the new data series will have terms

$$B_k = \frac{1}{M} \sum_{i=M \cdot k}^{M \cdot (k+1)} [\Lambda(t_i) + n(t_i)], \quad (20)$$

where  $B_i$  is the average value over the  $i^{\text{th}}$  minute of data,  $n(t_i)$  is the noise component,  $M$  is the total number of samples in a minute and  $k$  is the index for the downsampled data [10]. For actual LIGO data, this takes the sampling rate from 16384 Hz to 1/60 Hz.

Now we have removed the high frequency part of the signal, leaving just the AM and heterodyne error.

## 3 Data analysis

We now can simulate a signal with any particular ephemerides and we wish to find a signal buried within data. We can consider a time series of  $n$  data points as an element of an  $n$ -dimensional vector space. Therefore, in order to compare the similarities between two data sets of  $n$  elements, we can take their dot products in  $n$ -space. By using this metric for goodness of fit, we can choose the model which best replicates the data. Generating many template vectors, we can create a distribution across the entire parameter space which will have a maximum overlap value at the true parameters.

However, this analysis now must consider noise. The noise vector in  $n$ -space won't be perpendicular to our noise, so it will add some component to the statistic. This means that even in the absence of a signal, there will be

some overlap between the data and the template. As noise is random and approximately Gaussian (with mean and standard deviation understood from LIGO’s power spectral density and mean of zero), we can generate realistic models for this to understand how it affects the search for optimal parameters.

In order to find the conditions to maximize the dot product of the data and a model, we use probability theory. Bayes’ Theorem says that for two events A and B,

$$P(A|B) = \frac{P(B|A) \cdot P(A)}{P(B)}. \quad (21)$$

If we let A be the model and B be the data, eq. (21) says that the chance that the model is right given the data (what we wish to find) is equal to the probability of the data given the model (called the likelihood function) times the probability of the model (called the prior on A) divided by the absolute probability of the data being true (evidence). The evidence is difficult to compute, but it’s just a normalization constant. Therefore, eq. (21) will often be written as eq. (22):

$$P(A|B) \propto P(B|A)P(A). \quad (22)$$

The likelihood function is calculated via eq. (23).

$$l = e^{-\mathbf{d} \cdot \hat{\mathbf{d}}} \quad (23)$$

where  $\mathbf{d}$  is the given data variable and  $\hat{\mathbf{d}}$  is the expected data based on the model, A. This yields a Gaussian distribution centered around the best fit model.

The prior is considered by real-world observations or physical limits and usually takes the form of a Gaussian or a constant function over a region of the parameter space. For example, if one of the parameters for the model is strain amplitude, we know the strain will likely be around  $10^{-25}$  [8] but has no chance of being around  $10^{-1}$ . Therefore if a model is formed with strain  $10^{-1}$ , the prior should be 0, while a strain around  $10^{-25}$  should be assigned a moderately high prior value. We construct this distribution such that the prior is scale invariant, i.e. so it is uniform in log space.

The model dictates what parameters need to be searched over. In the simplest case, such as the Crab pulsar (where many of the parameters are well known from EM observations), we have at least 2 ( $h_0$  and  $\phi_0$ ) while we ultimately may have many more ( $\iota, \psi, \beta$ ). If we have  $m$  parameters, we have to search over an  $m$ -dimensional space.

If we were to sample over the entire domain of all  $m$  dimensions, we could get a probability distribution function (PDF) in  $m$ -space. The size of the parameter space grows with the number of dimensions, so just uniformly sampling over the entire space and taking a bunch of values is not computationally effective and is impacted significantly by the noise.

There are classical methods for choosing the parameters to do this, but we use an implementation of Markov Chain Monte Carlo (MCMC). This process involves a “mutation” cycle. Starting with randomly placed points across the

domain in  $m$  dimensions, we semi-randomly choose nearby points and compare similarity (via eq. (22)). If the second model has a higher likelihood than the first, the new point is saved. Otherwise, there is some chance that the new point will be saved, with probability based on how much lower the statistic is. Repeating this process a number of times yields a distribution of points which should represent the final PDF.

Generally though, we may not need the entire  $m$ -dimensional PDF, but a 1-dimensional one (e.g. we don't care about  $\phi_0$  but just want to know  $\beta$ ). To go lower in dimensions, we have to introduce the concept of marginalization. In a simple continuous case, we have a PDF that gives us the probability based on 2 parameters:  $\phi_0, h_0$ , given  $\mathbf{d}$ . To find the distribution for just  $h_0$  given  $\mathbf{d}$  (i.e. trying to find the distribution for the possible strain of the signal no matter what phase it's seen in), we integrate across  $\phi_0$  as below.

$$P(h_0|\mathbf{d}) = \int P(h_0, \phi_0|\mathbf{d}) d\phi_0 \quad (24)$$

This reduces by 1 dimension. If we start with  $m$  dimensions and repeat  $m - 1$  times, we will reduce the  $m$ -dimensional PDF to a 1 dimensional one. For this analysis, our multidimensional PDFs will be reduced to distributions in  $\beta$ , requiring marginalization over between 2 and 5 dimensions. We are ignoring any variance in other parameters (e.g. source position), since they have such tight distributions their PDFs would effectively be  $\delta$  functions.

## 4 Model creation

We created “toy models” for the key steps outlined above, using generic or standard assumptions. This was the basis for the deeper research.

In order to visualize the Rømer delay, one can plot it and find something like figure 3. It is significant that this is a sinusoid and that this has a non-negligible magnitude compared to our time resolution. Once we understand the delay, we want to plot the antenna patterns. We set  $\mathbf{d}_x$  and  $\mathbf{d}_y$  to be the  $x$  and  $y$  axes, with source position being arbitrary. Figure 4 shows the antenna patterns for  $+$  and  $\times$  and their sum, with no source polarization angle [11]. The distance from the center origin at any angle indicates the sensitivity of the detector to that polarization at that angular position relative to the detector arms (the  $x$  and  $y$  axes). It should be noted that the magnitude of subfigure 4.c is invariant under source rotation, as plus and cross polarizations are only different by a  $45^\circ$  rotation. These figures, while interesting, are not particularly useful in and of themselves. The sensitivity changes over a day because of the Earth's rotation. The antenna sensitivity depends on the positions of the observatory and the source (via eqs. 4 and 5). Showing this variation over a day, as well as the Rømer delay, for a sample source (Crab Pulsar) for both observatories then yields the plots in figure 5 for the AM  $\Lambda(t)$ .

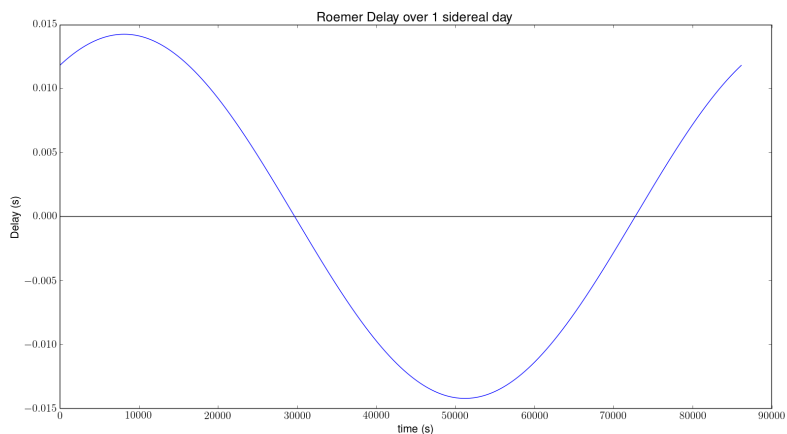


Figure 3: The Rømer delay over a sidereal day approximately makes a sinusoid, with smaller variations across a year.

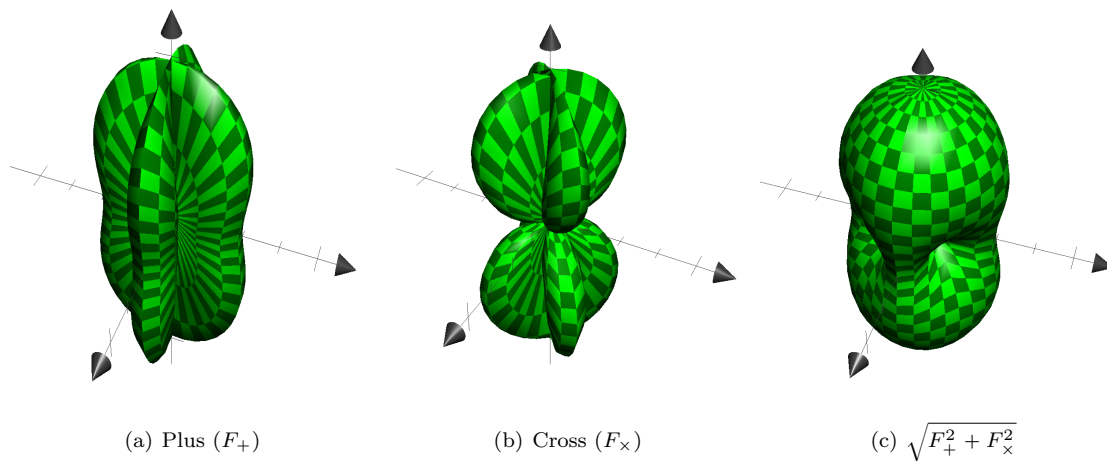
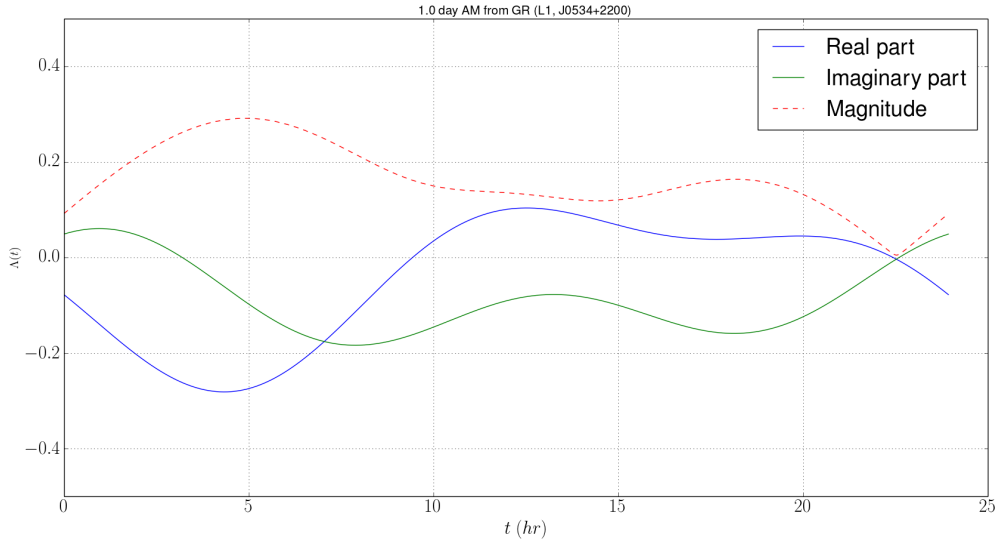
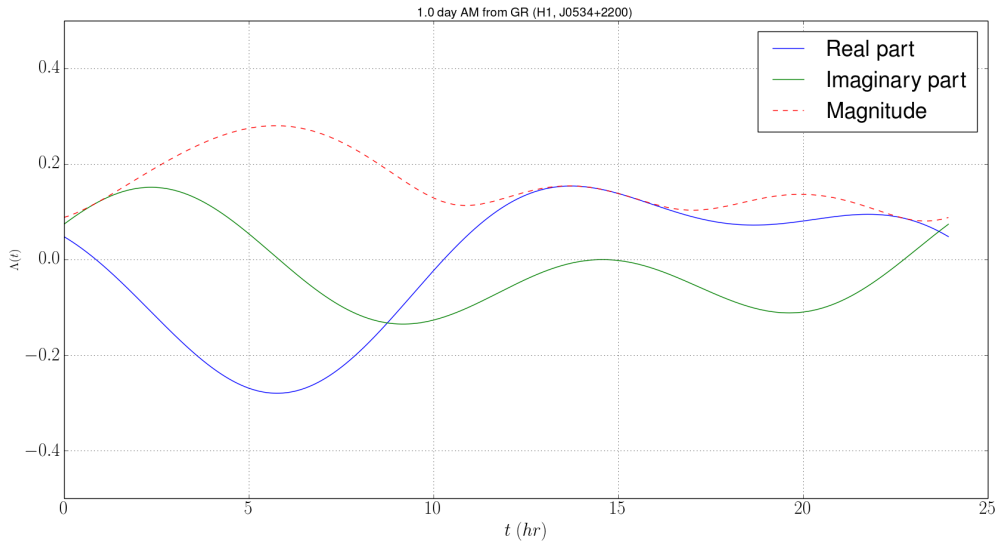


Figure 4: Antenna patterns for the two GR polarizations



(a)



(b)

Figure 5: Overall AM reaction to simulated Crab pulsar CW over a day at the (a) Hanford and (b) Livingston Observatories

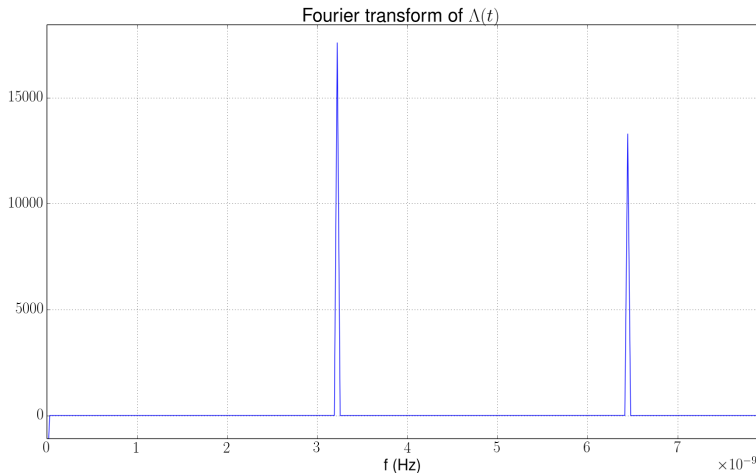


Figure 6: Fourier transform of the simulated  $\Lambda(t)$  for the Crab, zooming in on the barely noticeable bumps near 0; blue is real, green is imaginary. The three visible bumps represent an inherent term at frequency 0, the diurnal cycle at about 1/86164 Hz, and the twice diurnal cycle at about 1/43082 Hz. These plots agree with the official LIGO antenna patterns from LALSuite.

In order to check that this has the two frequencies we expect, we Fourier transform it. If we look closely, we can see the two frequencies we anticipate, as shown in Figure 6.

It is now useful to implement the mathematical concepts established using eqns.(8 - 20). To show this, we generated a day of a fake signal with amplitude modulation  $\Lambda(t) = 5 + \cos(\frac{2\pi t}{86164s})$  and fast sinusoid (signal) of  $h(t) = \Lambda(t) \cdot \sin(2\pi \cdot 0.01\text{Hz} \cdot t)$ . For this example, the GW frequency of 0.01 Hz is much lower than any pulsars in the LIGO band. The data are shown in Fig. 7.

The amplitude follows a sinusoidal progression with period about two times the length of its frame. Now, since we know the  $\theta(t)$  that we would plug into eq. (12), we can heterodyne to get figure 8. We can see the faster wave as well as the still slow wave in the amplitude modulation which equation 12 predicts.

Next, we take that data and downsample significantly (here, downsampling was by a factor of a few thousand), taking an average over every segment. This eliminates the high frequency data and leaves a signal at half of the amplitude of the waves, as seen in Fig. 9. In the above implementation there were some simplifications. The sinusoids were all constant in frequency, ignoring both  $\dot{\nu}$  and  $\ddot{\nu}$  terms. Generally, those would be included, on top of glitches. Glitches will mess with the smooth approximation, so have to be accounted for explicitly by time correlating the CW signal with radio observations. If  $c_g \approx c$ , the two should align quite well in time and allow us to use astronomical observations during the time of observation in order to model the frequency of the expected wave.

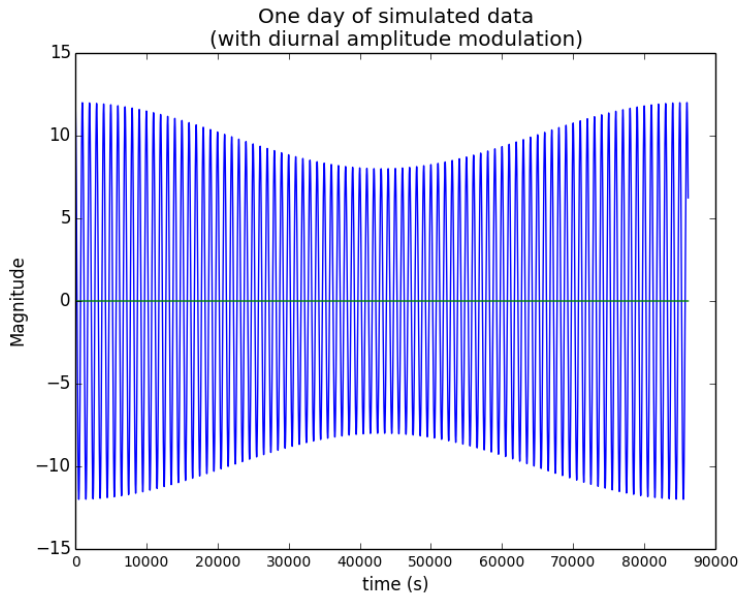


Figure 7: The simulated signal with  $\Lambda(t) = 5 + \cos\left(\frac{2\pi t}{86164s}\right)$  and  $h(t) = \Lambda(t) \cdot \sin(2\pi \cdot 0.01 \text{ Hz} \cdot t)$  for one day. Note the amplitude modulation. As a reminder, this represents a somewhat realistic model of a low frequency pulsar (0.05 Hz).

If  $c_g \ll c$ , this phase evolution may hurt the search, as it may expect glitches when none will exist but that case is not expected [12]. Furthermore, this model ignores the Rømer delay in order to simplify the visualization. Therefore the FM has zero impact here.

Implementing Rømer delays with variable values for  $\beta$  yields fig. 10. These waveforms will serve as our models. Here,  $h_0$  is 1 so the vertical scale is about 25 orders of magnitude above our expected signals.

Once we have the template, we want to start using MCMC in order to perform Bayesian inference on simulated data. We inject a nearly invisible signal and get PDFs that show that over a long period of time, we can detect significant changes.

## 5 Results

We implemented MCMC using the package `emcee` [13]. We searched across a parameter space of  $(h_0, \phi_0, \iota, \psi, \beta)$  to represent a pulsar with known position and frequency evolution. Although some sources have more constrained parameters, we assumed the case of most ignorance.

In order to make sure the system was functioning, we created an immensely loud signal that a functioning system should easily see. Using 3 days of simulated

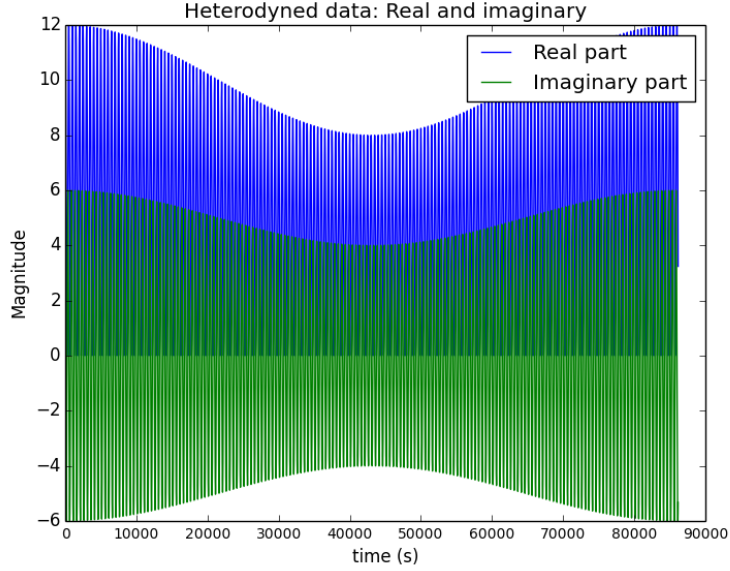


Figure 8: Heterodyne of the above data with known frequency evolution.

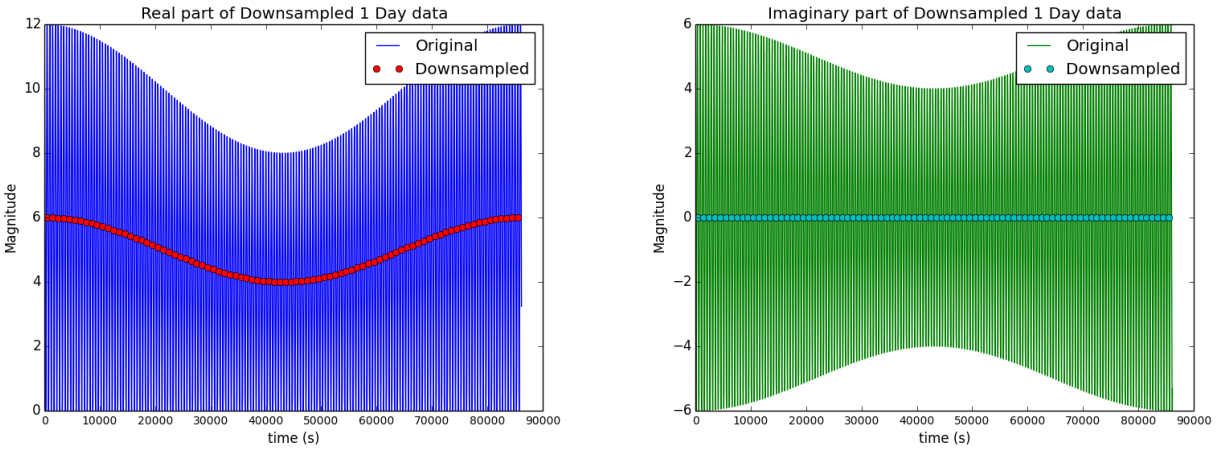


Figure 9: Real and imaginary parts of the downsampling from the heterodyned data. Note how the real part represents half of the amplitude of the final wave and the imaginary part goes to zero; this reflects the original data's purely real component.

data with  $\sigma_{\text{noise}} = 10^{-25}$  and  $h_0 = 7 \times 10^{-25}$  with Crab Pulsar parameters and

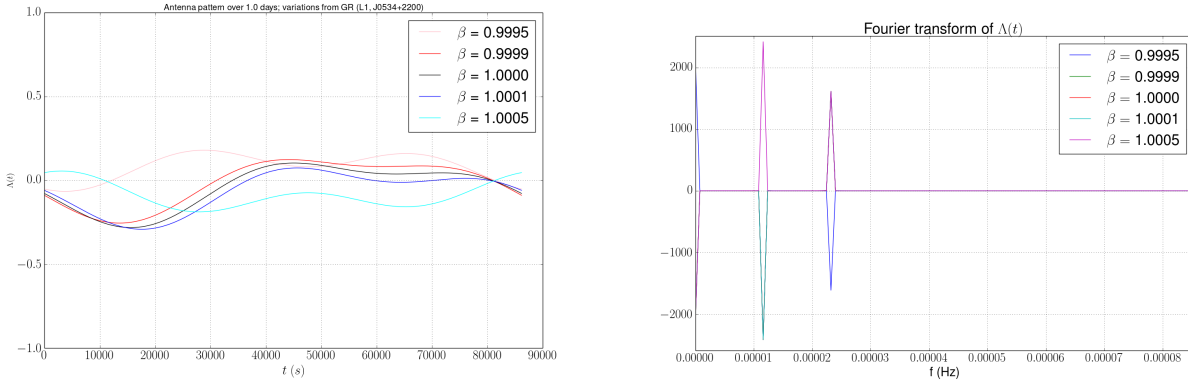
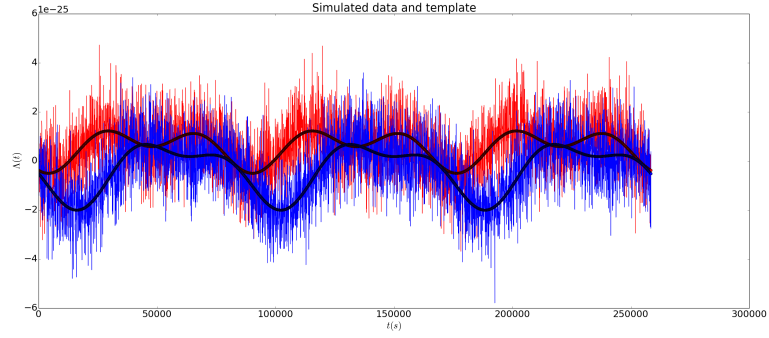
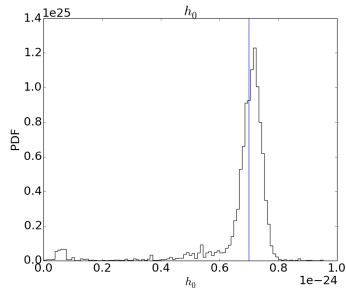


Figure 10: The first plot shows different waveforms that would be observed with  $c_g \approx c$ . The second is the Fourier transform of the first, showing their diurnal and semi-diurnal cycles.

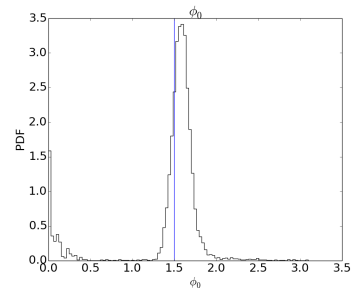
GR, we generated in the graphs below. This shows that the model is accurately finding all of these parameters.



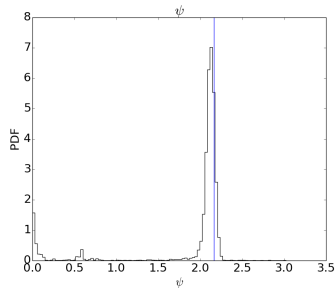
Simulated data for three days of operation (Downsampled and Heterodyned already)



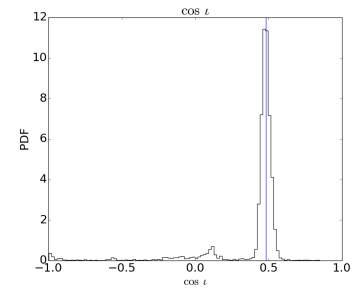
Strain parameter ( $h_0$ )



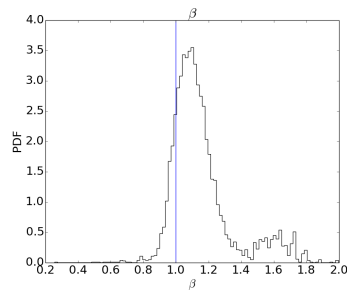
Phase angle ( $\phi_0$ )



Angle relative plane of view ( $\psi$ )



Cosine of inclination angle ( $\cos i$ )



Speed in terms of  $c$  ( $\beta$ )

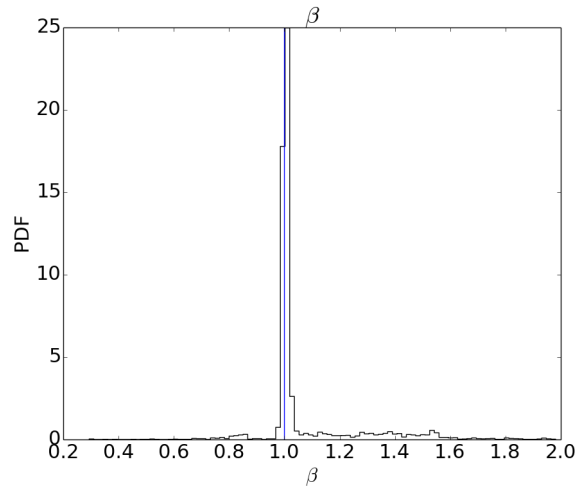


Figure 11: For 300 days of high SNR ( 1), we can very clearly find a strong measure of  $\beta$ ; Here, as in GR,  $\beta = 1$ .

With different parameters, we were also able to see other results:

1. Accuracy increased with more days (compare baseline to Fig. 11)
2. Non-GR results were still able to be accurately found (Fig. 12)
3. With many days, lower SNRs can still yield strong estimations of  $\beta$  (Fig. 13)
4. When combining the previous two examples, more significant spreading and overestimation come up (Fig. 14).

The increased spread of the PDF of  $\beta$  is likely a byproduct of the small effect of varying  $\beta$  and just noisy data. The systematic offset is due to an unknown mechanism, which should be analyzed in further research; whether it is a mistake in this implementation is unknown.

## 6 Future research

The next logical step in this research is to form more realistic models to analyze sensitivity to deviations from GR. We would begin by analyzing from simulated raw aLIGO data. By performing all of the analysis from the beginning of the process, we can reasonably check that the theory matches the implementation and yields similar results to this research. The framework established here also serves as a strong basis for that project. This realism can continue by using actual aLIGO noise instead of just assuming Gaussian noise, as found in LALSuite.

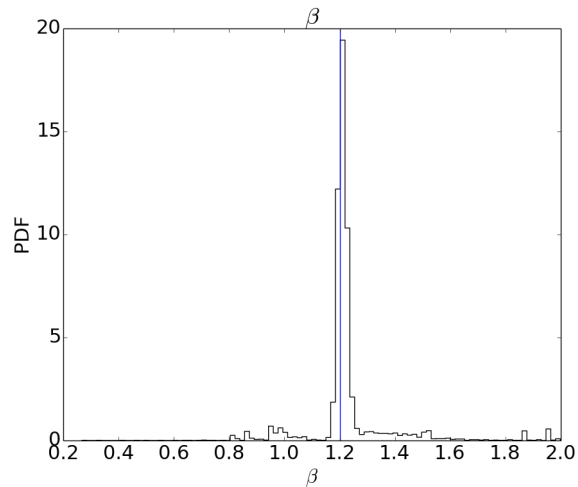


Figure 12: Implementing a large deviation from GR and observing over 300 days a signal with high SNR ( $\approx 1$ ),  $\beta$  was still recoverable (Note:  $\beta = 1.2$ , implying superluminal transmission of GWs)

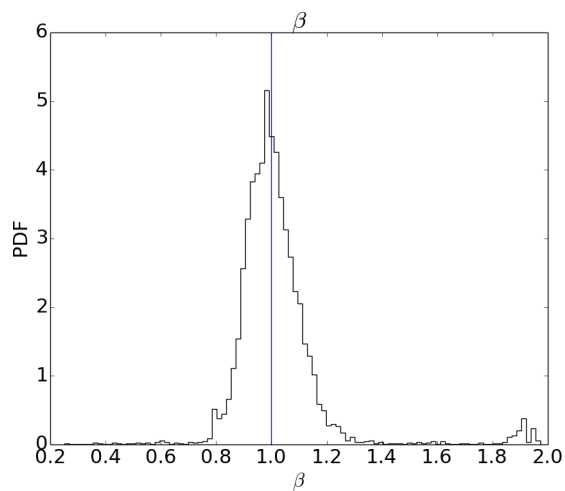


Figure 13: We repeat the test from Fig. 12 with a smaller SNR ( $\sigma_{\text{noise}} = 10^{-25}$  and  $h_0 = 7 \times 10^{-26}$ ). This shows a significantly greater variation, yet still centers around its true parameter ( $\beta = 1$ ).

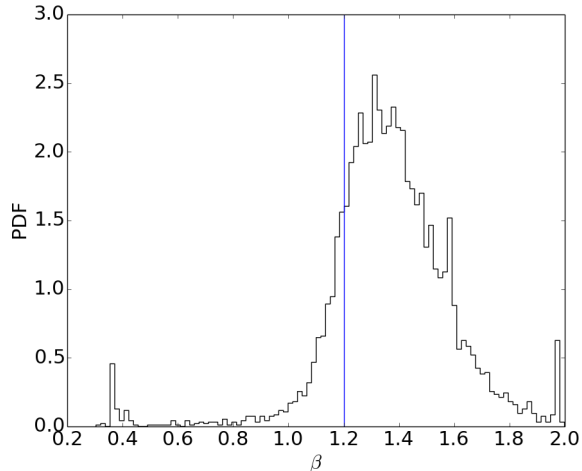


Figure 14: With a huge deviation from GR ( $\beta = 1.2$ ) and a long period 300 days with a low SNR (as in the Fig. 13),  $\beta$  was still somewhat recoverable, although the variance from the real parameter is significant. Similarly, the center of the distribution is not at the intended value.

Once we understand the ability to detect variances, we should investigate actual LIGO data, e.g. O1. We can analyze multiple known pulsars and create an infrastructure to accept differently dimensioned parameter spaces (e.g. pulsars with more known qualities like the Crab or less accurately known positions).

## 7 Acknowledgments

I want to sincerely thank the National Science Foundation, California Institute of Technology’s SFP office, and the SURF program for funding my work as well as the entire LIGO team. I would also like to mention my peers in the LIGO SURF program for emotional support and scientific inspiration.

More than anything, I’d like to acknowledge the immense support and guidance of my mentors, Maximiliano Isi and Professor Alan Weinstein. Without their assistance, I would not have learned nearly as much as I did.

## References

- [1] B.P. Abbott et al. Observation of gravitational waves from a binary black hole merger. *Physics Review Letter*, 116, 2016.

- [2] R.T. Edwards, G.B. Hobbs, and R.N. Manchester. TEMPO2, a new pulsar timing package - II. The timing model and precision estimates. 372:1549–1574, November 2006.
- [3] A. Teoh R.N. Manchester, G.B. Hobbs and AJ M. Hobbs. Web, 1993-2006 (2005).
- [4] M. Isi. Detecting deviations from general relativity using continuous gravitational waves (doc: T1300882). *LIGO*, 2013.
- [5] C. Mead M. Isi, A. J. Weinstein and M. Pitkin. Detecting beyond-einstein polarizations of countinuous gravitational waves. *LIGO*, 2015.
- [6] Atsushi Nishizawa et al. Probing nontensorial polarizations of stochastic gravitational-wave backgrounds with ground-based laser interferometers. *Physical Review Letters*, 79, 2009.
- [7] Mark Zimmermann and Eugene Szedenits. Gravitational waves from rotating and precessing rigid bodies: Simple models and applications to pulsars. *Phys. Rev. D*, 20:351–355, Jul 1979.
- [8] Edwin F. Taylor and Edmund Bertschinger. *Exploring Black Holes: Introduction to General Relativity 2nd ed.* Addison Wesley Longman, San Francisco, 2000.
- [9] Max Isi Colin Gill Matthew Pitkin, John Veitch. Pulsar parameter estimation file reference. [software.ligo.org/docs/lalsuite/lalapps](http://software.ligo.org/docs/lalsuite/lalapps).
- [10] Matthew Pitkin. *Prospects of observing continuous gravitational waves from known pulsars*. PhD thesis, California Institute of Technology, 2011.
- [11] Max Isi et. al. Detecting beyond-einstein polarizations of continuous gravitational waves. *LIGO*, April 2015.
- [12] Matthew Pitkin Garth S. Davies and Graham Woan. A targeted spectral interpolation algorithm for the detection of continuous gravitational waves. 2016.
- [13] Dan Foreman-Mackey & contributors. Emcee documentation. <http://dan.iel.fm/emcee/current/>.